metals

MDPI

Article

Additive Manufacturing and Precipitation Hardening of Low-Alloyed Copper Alloys Containing Chromium and Hafnium

Julia Dölling [1,*], Samira Gruber [2], Felix Kovermann [3], Lukas Stepien [2], Elmar Beeh [1], Elena Lopez [2], Christoph Leyens [2], Hans-Günther Wobker [3] and Andreas Zilly [4]

[1] Institute of Vehicle Concepts, German Aerospace Center e.V. (DLR), Pfaffenwaldring 38–40, 70569 Stuttgart, Germany; elmar.beeh@dlr.de
[2] Fraunhofer Institute for Material and Beam Technology (IWS), Winterbergstraße 28, 01277 Dresden, Germany; samira.gruber@iws.fraunhofer.de (S.G.); lukas.stepien@iws.fraunhofer.de (L.S.); elena.lopez@iws.fraunhofer.de (E.L.); christoph.leyens@iws.fraunhofer.de (C.L.)
[3] cunova GmbH, Klosterstraße 29, 49074 Osnabrück, Germany; felix.kovermann@cunova.com (F.K.); hans-guenter.wobker@cunova.com (H.-G.W.)
[4] Faculty of Technology, Cooperative State University Stuttgart, Lerchenstraße 1, 70174 Stuttgart, Germany; andreas.zilly@dhbw-stuttgart.de
* Correspondence: julia.doelling@dlr.de

Abstract: Copper alloys with chromium and hafnium offer the possibility of precipitation hardening and combine enhanced strength with high electrical and thermal conductivities. The production process, which starts with raw materials, involves powder production by gas atomization and leads to additive manufacturing by laser powder bed fusion with different parameter sets. The aim is to utilize precipitation reactions afterwards in CuHf0.7Cr0.35 during temperature exposure for further property optimization. This research focuses on the low-alloyed copper alloy with hafnium and chromium, compares this with conventionally manufactured specimens, and relates the alloy to additively manufactured specimens of other benchmark alloys such as CuCr1Zr. Measurements of hardness and electrical conductivity are accompanied by metallographic investigations to understand the behavior of CuHf0.7Cr0.35 manufactured by generative methods. In the as-built condition, melting traces remain visible in the microstructure, and hardness values of 101 HV and an electrical conductivity of 17.5 MS/m are reached. Solution annealing completely recrystallizes the microstructure, and the following quenching holds further alloying elements in supersaturated solid solution, resulting in 73 HV and 16.5 MS/m. Subsequent target-oriented precipitation reactions enable peak values of about 190 HV and 42 MS/m. Future research will assess mechanical and physical properties at elevated temperatures and evaluate possible applications.

Keywords: laser powder bed fusion; short wavelength laser system; copper–hafnium CuHf; copper–chromium CuCr; precipitation hardening; conductivity improvement

Citation: Dölling, J.; Gruber, S.; Kovermann, F.; Stepien, L.; Beeh, E.; Lopez, E.; Leyens, C.; Wobker, H.-G.; Zilly, A. Additive Manufacturing and Precipitation Hardening of Low-Alloyed Copper Alloys Containing Chromium and Hafnium. *Metals* **2024**, *14*, 1304. https://doi.org/10.3390/met14111304

Academic Editor: Bo Song

Received: 17 October 2024
Revised: 11 November 2024
Accepted: 16 November 2024
Published: 19 November 2024

1. Introduction

High-performance applications require copper alloys with high electrical and thermal conductivities and also high strength at elevated temperatures. Hardening by the nucleation and growth of precipitates enables a beneficial combination of high strength, higher ductility, and increased conductivity.

Alloying elements enabling precipitation hardening have a limited solubility in the copper (Cu) matrix, which decreases with temperature [1]. In terms of the electrical and thermal conductivities, all solute alloying elements in the copper matrix metal significantly scatter conduction electrons and result in unfavorably low values [2–4]. Therefore, low-alloyed precipitation hardening copper alloys are the focus of this research. As an industrial benchmark alloy, CuCr1Zr is investigated in direct comparison with a low-alloyed ternary

option in the CuHfCr system. In particular, the additive processing of this alternative alloy containing hafnium (Hf) and chromium (Cr) has not yet been investigated. Referring to the already published precipitation behavior of CuHfCr alloys, their mechanical and physical properties are promising [5–7]. Therefore, the transfer from cast and further processed semi-finished products to the additive manufacturing (AM) method is the next step to further explore the potential of alternative copper alloy systems.

1.1. Precipitation of CuHfCr Alloys

Chromium, at 0.65 wt.% at 1075 °C, has a limited solubility in copper, decreasing with temperature [8]. With a similar atomic radius, the alloying element readily diffuses into the matrix metal, resulting in rapidly and continuously growing precipitates [2,9]. These mainly Cr-containing precipitates (growth-capable nuclei are of fcc structure and later progress to the bcc structure [8,10,11]) are assumed to be of spherical shape [12]. The associated strengthening mechanisms include the shear and Orowan mechanisms in earlier coherent and later incoherent precipitates [10,13–17]. The addition of small amounts of zirconium (Zr) to CuCr alloys results in reduced growth of the predominantly Cr-containing precipitates [18] and minimizes the risk of embrittlement at intermediate temperatures due to grain boundary segregation [19]. Zr atoms tend to diffuse into the boundary zone and thus prevent coarsening of the predominantly Cr-containing precipitates [18,20,21]. As a result, the strength of the alloy at elevated temperatures is increased, and creep and relaxation effects are reduced [22–24]. In summary, precipitation effects in CuCr and CuCrZr alloys have been the subject of several scientific investigations for decades and continue to be so due to their industrial relevance.

Hafnium shows a maximum solubility of 0.84 wt.% at 963 °C in copper [25]. In these alloys, the precipitating phase is considered to be the intermetallic compound Cu_5Hf [25–28], which follows a precipitation process to form rod-like structures that grow during aging [29,30]. The advantageous mechanical properties of binary CuHf alloys with minor sacrifices regarding the conductivity [2,31–33] led to further investigation of ternary alloy systems [5,7,26–28,34–40].

The addition of Hf to ultra-fine-grained (UFG) microstructures of CuCr1Zr increases the recrystallization and softening temperature [25,34,39,40]. Therefore, it is important to understand interactions and influences on the precipitation behavior of ternary CuHfCr alloys [5,34]. The mechanical properties of CuHfCr alloys significantly exceed those of binary versions and the benchmark material CuCr1Zr [5,6]. In contrast to binary CuHf alloys, the addition of Cr enables accelerated precipitation reactions in solution-annealed specimens and reduces the need for facilitating cold-rolling prior to aging [5,6]. At aging temperatures between 400 °C and 500 °C, mainly Cr-containing precipitates of about 5 nm to 15 nm nucleate and grow. Hf atoms segregate at the interface between these precipitates and the surrounding matrix, resulting in the nucleation of intermetallic CuHf phases that grow in elliptical shapes of about 20 nm to 40 nm in length [5,6]. This results in finely distributed small precipitates that allow good electrical and thermal conductivities as well as high mechanical properties at room and elevated temperatures [6].

1.2. Additive Manufacturing of High-Perfomance Copper Alloys

Additive manufacturing (AM) of copper-based materials has gained attention in recent years [41,42]. Processes such as laser powder bed fusion (PBF-LB/M) and electron beam melting (PBF-EB/M) are the focus of investigations for the manufacturing of copper and various low-alloyed precipitating alloys such as CuCr1Zr and CuNiSi [43,44]. PBF-LB/M produces parts with high relative densities of approximately 97.5% to 99.5% that can be further optimized by subsequent hot isostatic pressing or other post-processing [45]. The rapid melting and solidification (heating/cooling rates: ~10^3 to 10^8 K/s) results in high supersaturation and a significantly different microstructure compared to conventional manufacturing methods [46].

Processing copper and copper alloys with commercial PBF-LB/M machines using an infrared laser has historically been challenging due to the low absorption rate of laser radiation in copper at the infrared wavelength and the high thermal conductivity of the material. There have been two approaches to overcome this challenge: 1. increasing the IR laser power to 1000 W [47] or 2. changing the laser source to a green wavelength where the absorption is significantly higher [42,48]. Heat treatments after additive manufacturing result in a significant increase in the electrical conductivity and mechanical properties of these precipitable alloys [43,45,49,50].

The use of these alloys is advantageous due to their excellent mechanical properties and high electrical and thermal conductivities, which make them ideal for nuclear and aerospace industries [41]. AM, with its high design freedom, is particularly suitable for monolithic designs of, e.g., injectors, ignition mechanisms, nozzles, or combustion chambers with complex optimized internal cooling channels [51,52].

For high performance applications, CuCrZr or CuNiSi alloys are used with optimized aging treatments and targeted precipitation reactions [52]. Furthermore, GlidCop alloys, mainly processed in EBM processes, are in the family of oxide dispersion-strengthened copper alloys (ODS-Cu) [53]. These reach the desired mechanical properties by the dispersion of fine alumina particles [53] and are consequently not heat treatable but suited for elevated operation temperatures. In particular, CuCrZr alloys are currently processed with AM and tested in the aerospace sector and are convincing due to their simple and high-quality powder production [52]. PBF-LB/M-processed CuCr1Zr with subsequent direct aging resulted in a hardness of 184 HV1, a yield strength of 527 MPa, an ultimate tensile strength of 585 MPa and an electrical conductivity of 40 MS/m [54,55]. In the as-built condition, a hardness of 85 HV in combination with an electrical conductivity of 11 MS/m was achieved and after solution annealing, the hardness was reduced to 65 HV while maintaining the conductivity [46]. Direct aging between 400 and 600 °C for up to 12 h resulted in higher hardness values of 190 HV and 42 MS/m, whereas solution annealing and aging resulted in lower hardness values of 130 HV but a higher conductivity of 47 MS/m [46].

CuCrNb alloys are being developed by NASA for reusable combustion engines (GRCop-84 or -42 [56–58]). These alloys form the highly stable intermetallic phase Cr_2Nb and increase the strain and fatigue capabilities compared to other copper alloys but significantly increase the cost due to the high effort required for powder production [52,59]. In direct comparison, the GRCop-42 appears to be more suitable for powder atomization than GRCop-84 due to the lower alloying content of Cr and Nb [60], but CuCr1Zr and other alloys are even simpler in terms of powder production.

In this context, heat treatments at moderate temperatures are favorable to minimize warpage phenomena [49,50] in the case of near-net-shape components of larger complex structures. Due to the high solidification and fast cooling rates during powder atomization and the AM process, the need for solution annealing can be questioned and discussed for the individual materials. Less energy consumption, less oxidation, and less warpage can be achieved if the precipitation reactions are directly activated in the as-built condition. Nevertheless, a supersaturated solid solution of alloying elements is the necessary precondition for subsequent precipitation reactions, increasing conductivity values and improving mechanical properties. For CuCr1Zr, in most cases, the solution annealing process still offers advantages for the resulting mechanical properties especially for ductility, compared to direct aging [53]. Finally, this influence needs to be discussed within the individual alloy, powder morphology, and AM process, which is the focus of this investigation as well.

Overall, alloys of the CuHfCr system have a high potential for additive manufacturing processes, as they enable advantageous combinations of properties and effective precipitation hardening. Neither research regarding the atomization of such alloys nor the processing via PBF-LB/M has been conducted. After introducing the utilized materials and methods, the results including their discussion follows in a technologically sequential order. First, the atomized spherical powder and its microstructure is analyzed and appears to be well suited for additive manufacturing. Second, two different parameter sets for the

additive manufacturing process are compared regarding the resulting density, material properties, and microstructure. Slight differences are investigated and can be attributed to the manufacturing parameters. The higher laser scanning velocity can be assigned advantages with regard to a manufacturing strategy. Furthermore, solution annealing enables recrystallization of the microstructure of the specimen and fully solubilizes alloying elements in the copper crystal. These results are contrasted with the casted specimen of the CuHf0.7Cr0.35 alloy and emphasize the promising properties of the additively manufactured specimen. In the following section, aging treatments are investigated and the resulting properties are contrasted in detail. Material properties, such as hardness and electrical conductivity, can be adjusted through targeted aging heat treatments. Finally, conclusions regarding beneficial manufacturing strategies can be drawn and build a basis for further characterization and investigation of occurring mechanisms.

2. Materials and Methods

2.1. Specimen Production by Casting Technology

Specimens with 500 g casting weight were produced using a VC400 gravity die casting machine (Indutherm Blue Power Casting Systems, Walzbachtal, Germany). The raw materials Cu-OFE as well as the master alloys CuHf60 and CuCr10 were heated and melted under vacuum conditions in a boron nitride-coated graphite crucible. After homogenization and electromagnetic stirring of the melt at 1300 °C, the metal was cast in a graphite die (5 mm thick bar) under vacuum conditions.

The cast specimens were then solution annealed at 970 °C for 120 min in a preheated furnace (ME65/13, Helmut ROHDE GmbH, Prutting, Germany) followed by manual quenching to room temperature in a circulating 60 l reservoir containing water (corresponding to the manufacturing processes of Doelling et al. [5,61]). Aging heat treatments at 475 °C followed for target-oriented precipitation hardening.

Including information about the cast specimens is not the main focus of this discussion but is a worthy consideration for analyzing proportions and conducting plausibility comparisons.

2.2. Specimen Production by Additive Manufacturing

Figure 1 visualizes the manufacturing process of the specimens, starting with the raw materials for powder atomization, through the PBF-LB/M process to heat treatments.

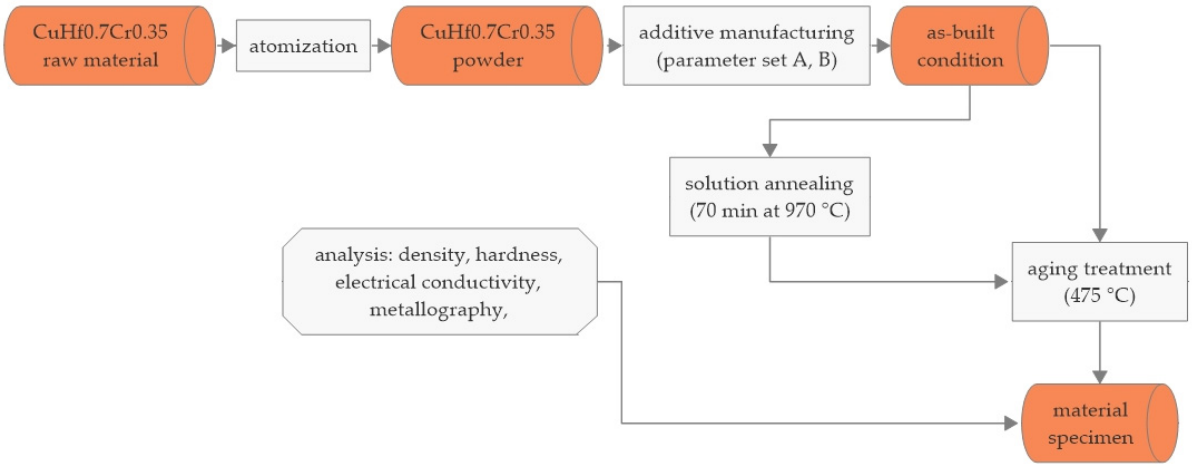

Figure 1. Flowchart of specimen manufacturing including utilized methods for material analysis.

2.2.1. Powder

A VIGA atomizer with a closed-coupled vaporizer was used to produce the powder. For melting, the raw materials were heated under an inert Ar atmosphere. After homogenization and electromagnetic stirring, the metal was atomized. During this process, the melt solidifies with very high cooling rates up to 10^6 K/s [62], resulting in fine powder particles.

After atomization, the powder was screened to separate into coarse fractions (above 63 µm particle size) and wind sifted to separate the fine fraction (below 10 µm) to achieve the desired particle size between 10 and 63 µm.

2.2.2. Additive Manufacturing

Several 10 mm high cuboids were produced using PBF-LB/M. The base areas were 10 × 10 mm, 15 × 10 mm, and 20 × 10 mm rectangles. Two different manufacturing parameter sets were tested:

- Parameter A: laser power 500 W, laser scanning velocity 600 mm/s, hatch distance 150 µm, and a layer thickness of 30 µm
- Parameter B: laser power 500 W, laser scanning velocity 1100 mm/s, hatch distance 150 µm, and a layer thickness of 30 µm

All specimens were manufactured on a TruPrint 1000 Green Edition (TRUMPF GmbH + Co. KG (Holding), Ditzingen, Germany) with an integrated TruDisk1020 disk laser (wavelength of 515 nm, maximum laser power 500 W). Figure 2a visualizes the schematic machine with process-relevant components. As a baseplate, a steel plate with 100 mm diameter was used (Figure 2b).

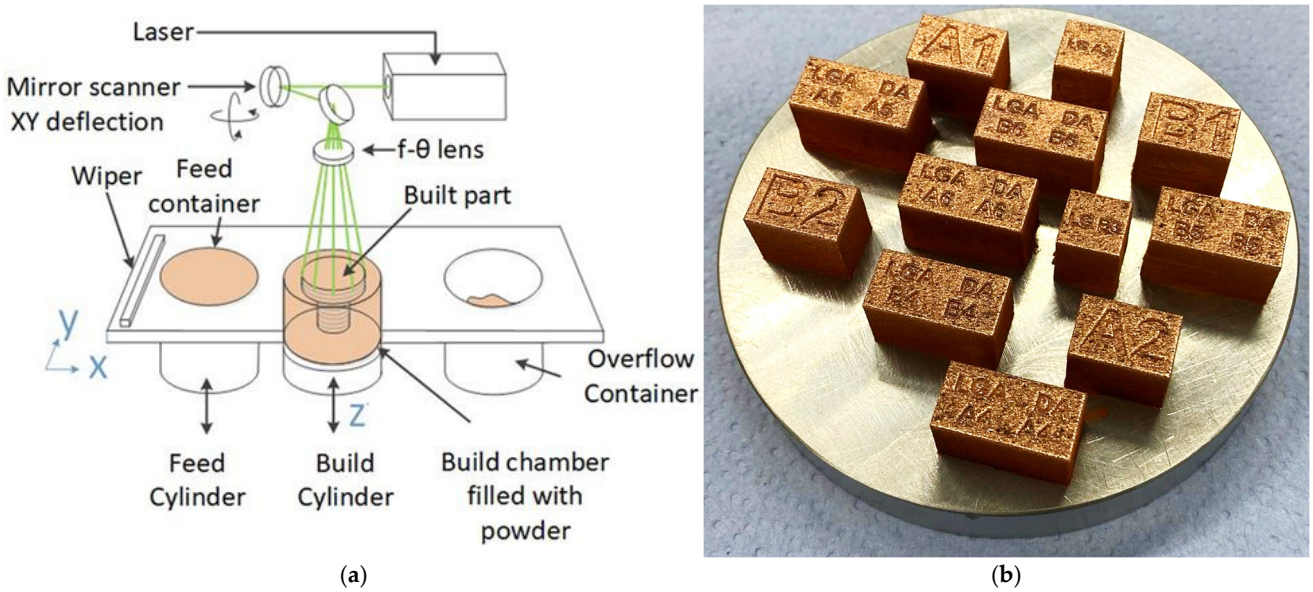

(**a**) (**b**)

Figure 2. Additive manufacturing of the specimens: (**a**) schematic visualization of a PBF-LB/M process utilizing a green laser source (reprinted from Ref. [58]); (**b**) density cuboids on the steel-built plate.

For the following investigations, the cross-section was defined in the x-y plane, whereas the longitudinal sections were defined in the x-z and y-z planes.

2.2.3. Heat Treatment: Solution Annealing and Aging

Half of the specimens were annealed after the printing process at 970 °C for 70 min followed by water quenching to room temperature. For aging, as-built samples and solution-annealed samples were heat treated at 475 °C for 2, 4, and 8 h with air cooling.

2.3. Methods for Analysis

2.3.1. Alloy Composition

The alloy composition was analyzed with a calibrated optical emission spark spectrometer (Spectrotest, SPECTRO Analytical Instruments GmbH, Kleve, Germany) on grinded cross sections. For the target composition of CuHf0.7Cr0.35, a maximum deviation of 0.05 wt.% within 10 measurements was accepted. For the cast specimens, the analysis

was conducted for the solution-annealed condition. In the case of the copper alloy powder, the material composition was determined in the printed condition of the additive manufactured cuboids (Figure 2b).

2.3.2. Material Properties

The electrical conductivity was measured using a calibrated eddy current test (Sigmascope SMP10, with TF100A for temperature compensation, Helmut Fischer GmbH, Sindelfingen, Germany). The specimens were analyzed in their cross sections with a grinded surface (SiC paper, grit 800, Schmitz-Metallographie GmbH, Herzogenrath, Germany) at a measurement frequency of 60 kHz. Seven measurements were averaged on each surface.

The mechanical properties of the specimens were characterized using a hardness tester (HV0.1) (NEXUS 412A equipped for DIN EN ISO 6507-1:2018 [63] Vickers hardness test, Innovatest GmbH, Selfkant-Heilder, Germany). Five measurements were averaged.

The measurements of hardness and electrical conductivity were measured in the x-z plane parallel to the build direction of the specimens.

The densities of the cuboids were measured by the Archimedes method in distilled water using a Satorius Entris II and the density measurement set YDK03 (Satorius AG, Göttingen, Germany) allowing a measurement accuracy of 0.1 mg. Measurements were conducted on five cuboids each. MatCalc version V6.04 was used to calculate the theoretical density of the alloy material at room temperature.

2.3.3. Metallographic Investigations

Scanning electron microscopy (SEM) was used for the loose powder material and printed and cast specimens (Gemini Sigma VP with the used NTS BSD (Carl Zeiss Microscopy Deutschland GmbH, Oberkochen, Germany) and XFlash 6 | 30 detectors (Bruker Nano GmbH, Berlin, Germany)). For acceleration of the electrons, 10 kV was used in combination with the 120 µm aperture. Lower magnifications were investigated with light microscopy (DM2700DM, Leica Microsystems, Wetzlar, Germany). For this purpose, some specimens were etched corresponding to Klemm III [64].

Furthermore, the powder morphology and the particle size distribution were analyzed via dynamical digital image distribution according to ISO 13322-2 [65] (CAMSIZER X2, Microtrac Retsch GmbH, Haan, Germany). For the analysis of CuHf0.7Cr0.35, about 3.2 million particles were analyzed in the basis program and about 400,000 particles in the detailed zoom analysis with 10,000 images each.

3. Results and Discussion

3.1. Powder and Alloy Analysis

The particle size distribution of the atomized CuHf0.7Cr0.35 powder is visualized in Figure 3. Such a distribution can be described with a Poisson distribution. Overall, D10 was measured and calculated at approximately 13.24 µm, D50 at approximately 32.54 µm, and D90 at approximately 55.53 µm. The sphericity of the particles was determined to be 0.916.

SEM investigations confirmed the mainly spherical shape of the CuHfCr alloy particles, as shown in Figure 4. Furthermore, the powder had only a low number of agglomerated particles, and only some particles were surrounded with one to two satellites. As a consequence, this powder is well useable for PBF-LB/M [60].

Additionally, no internal pores were observed, which became visible in the grinded and polished powder specimens of Figure 5, and the spherical shape of particles with an average diameter of about 30 µm was confirmed by manual measurement of individual particles. According to the already known behavior of hafnium in cast CuHfCr alloys [5,6], the element Hf tends to agglomerate in intergranular spaces. Utilizing the backscatter detector, the brighter structures visible in Figure 5 can be referred to an elevated Hf concentration. Consequently, further outcomes concerning the particles the microstructure were possible. The cooling and solidification during the atomization process enabled high temperature gradients and fast cooling rates, resulting in a fine-grained microstructure.

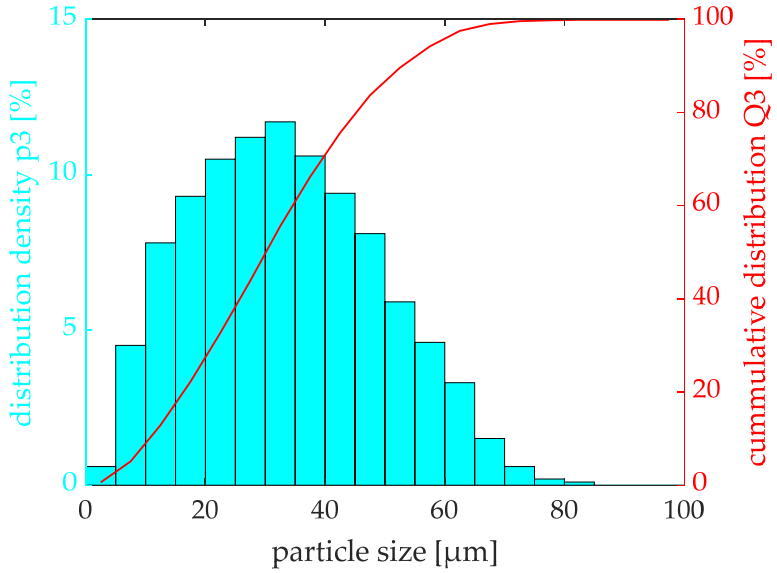

Figure 3. Particle size distribution of CuHf0.7Cr0.35.

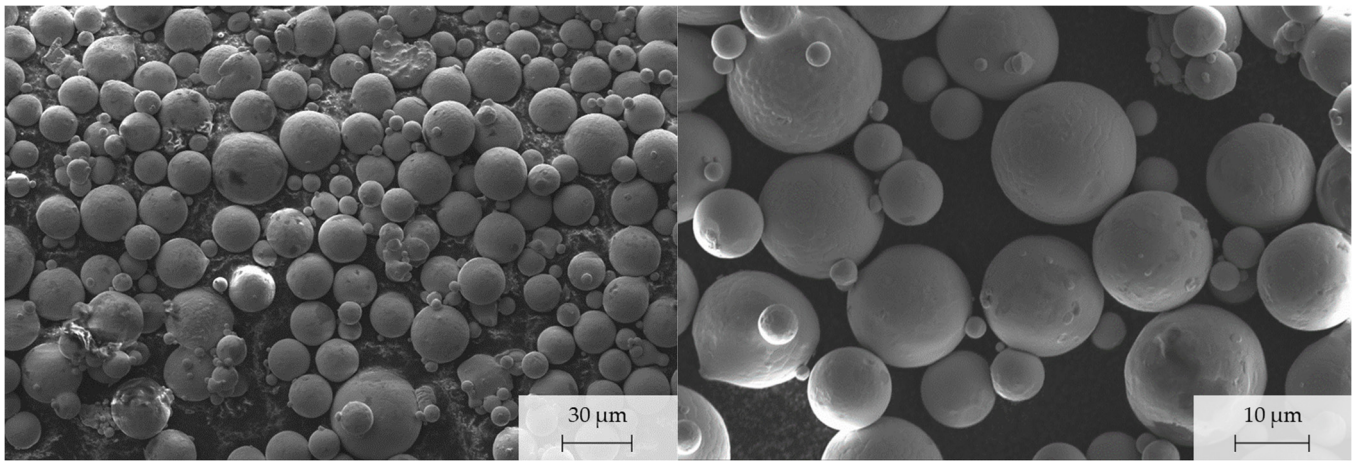

(**a**) (**b**)

Figure 4. Loose powder of CuHf0.7Cr0.35 alloy in overview (**a**) and detail (**b**).

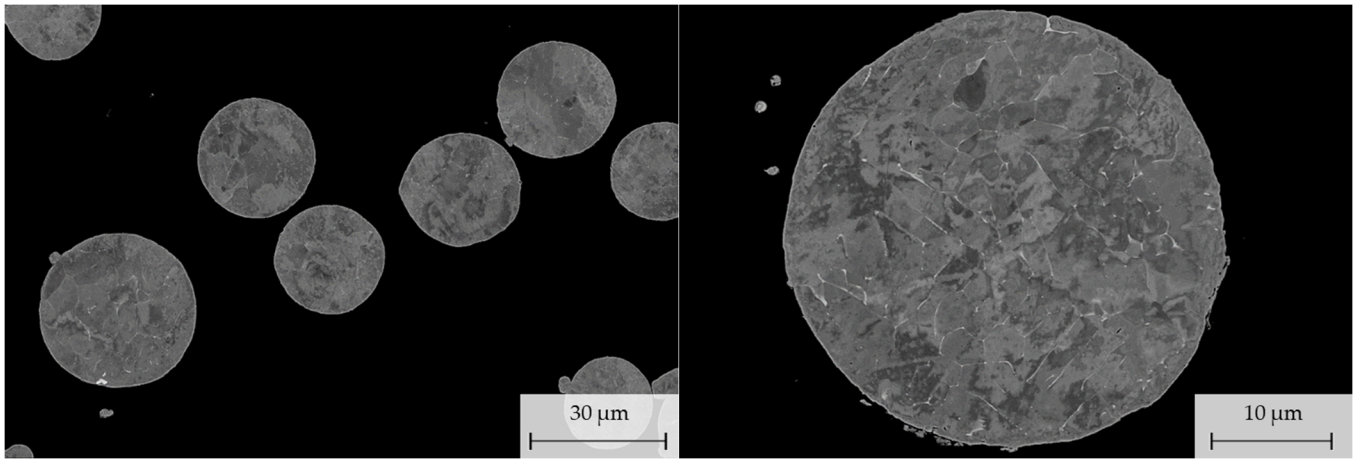

(**a**) (**b**)

Figure 5. Grinded and polished powder particles (**a**) revealing the microstructure in the particles of CuHf0.7Cr0.35 (**b**).

During the powder analysis, several particles with different compositions were present showing different microstructures (see Figure 6). Most particles were comparable to the microstructure of Figure 6a, but some particles revealed a significantly different microstructure of Hf-rich concentrations (Figure 6b). Integral EDS analysis of the particle surface of Figure 6a indicated concentrations of 0.60 wt.% Hf and 0.31 wt.% Cr. Measured on 25 particles located next to each other stochastically, the average alloy composition was 0.81 wt.% Hf and 0.29 wt.% Cr.

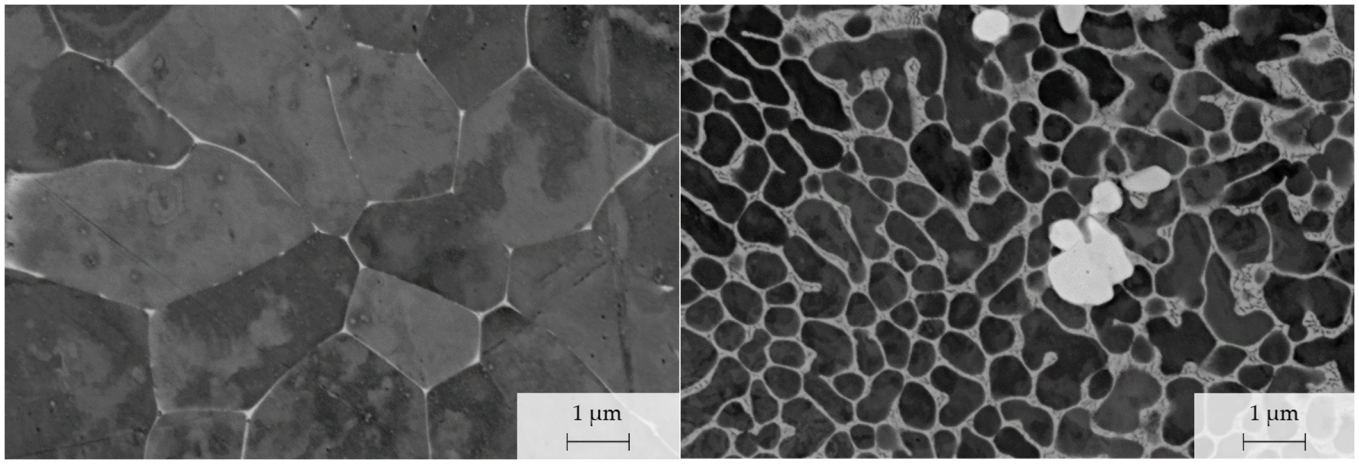

(**a**) (**b**)

Figure 6. Grinded and polished powder particles of CuHf0.7Cr0.35 in the BSD with different concentrations of Hf and Cr: lower Hf concentrations (0.31 wt.% Cr, 0.60 wt.% Hf, Cu balance) (**a**) and higher Hf concentrations (4.33 wt.% Hf and 0.26 wt.% Cr) (**b**).

Apart from single-particle element concentrations, the overall element concentrations in the cuboids, both cast and additively manufactured, were measured using spectral analysis and are summarized in Table 1. During the measurements at different positions on the additively manufactured cuboids surfaces and cross sections, the maximum deviation was below 0.02 wt.%.

Table 1. Concentrations of chromium and hafnium in the copper alloys of specimens produced by casting and AM.

Specimen	Cr [wt.%]	Hf [wt.%]
cast CuHfCr	0.28	0.69
AM CuHfCr	0.35	0.63

Generally, the cast and additively manufactured specimens' chemical compositions were comparable.

3.2. Investigation of the As-Built-Condition and the Solution-Annealed Condition

The main focus of this investigation was the analysis of CuHfCr specimens and their behavior at two different manufacturing parameter sets. Whereas parameter set B was in correlation with the previously investigated manufacturing of CuCr1Zr, parameter set A had parallels with the manufacturing of GRCop materials [58]. In addition, some first insights and direct comparisons to solution-annealed conditions were gained.

To assess the quality of the as-built condition and the suitability of production parameters, the density and porosity of density cuboids were the focus of first investigations. Copper solid solution and Cu_5Hf were present at room temperature in thermodynamic equilibrium, investigated in-depth with MatCalc. The calculated density was approximately 9.108 g/cm^3. Table 2 visualizes the density calculated by the Archimedes' principle in direct comparison. With 97.9% and 97.7% relative densities for A and B, respectively,

both production parameter sets resulted in good absolute densities that are comparable with densities of other PBF-LB/M processes utilized for copper alloys [45]. Furthermore, the Student's *t*-test (performed with $\alpha = 0.05$ and similar variances) results did not indicate any statistical difference between the two parameter sets. Influence of capillary effects at the rough surface of specimens could have influenced the measurement of the specimens with an average mass (at the atmosphere) of 10 g. Consequently, metallographic investigations followed to analyze internal pore size and shape.

Table 2. Densities determined by Archimedes' principle referred to the theoretical calculations with MatCalc and microscopic gray scale analysis of the core porosities measured on six surfaces each.

	Parameter A	**Parameter B**
measured Archimedes density [g/cm^3]	8.917 ± 0.025	8.896 ± 0.062
relative density [%] (Archimedes and MatCalc)	97.9	97.7
microscopic area fraction of core pores [%]	0.0163 ± 0.0076	0.0778 ± 0.0198
core pore size [µm]	27.27 ± 11.59	24.28 ± 13.47
maximum core pore size [µm]	43.50 ± 18.84	83.70 ± 28.18

Grayscale investigations of five surface areas in total each indicated comparable pore areas of 0.02% and 0.08% as well as comparable core pore sizes for both parameter sets (Table 2). Both parameter sets resulted in high material density in the additively manufactured as-built condition of the CuHf0.7Cr0.35 alloy. Production parameter set A resulted in slightly less core porosity and a higher density. In direct comparison with CuCr1Zr alloys manufactured in a comparable powder production and further AM processes, relative densities of 93–99.8% were achieved utilizing different laser power, scanning speed adjustments [55,62], scanning strategy, hatch distance, and remelting management, with high impact on the resulting densities [54].

Further optimization of the process parameters for CuHfCr could also improve the overall density and reduce pore sizes. For the pore analysis, computed tomography could be used in the future to understand the shape and distribution of pores in the printed cuboids.

In the as-built condition, melting tracks are visible in Figure 7c,d (marked with arrows), which correlate with the chosen the layer thickness of 30 µm in the additive manufacturing process.

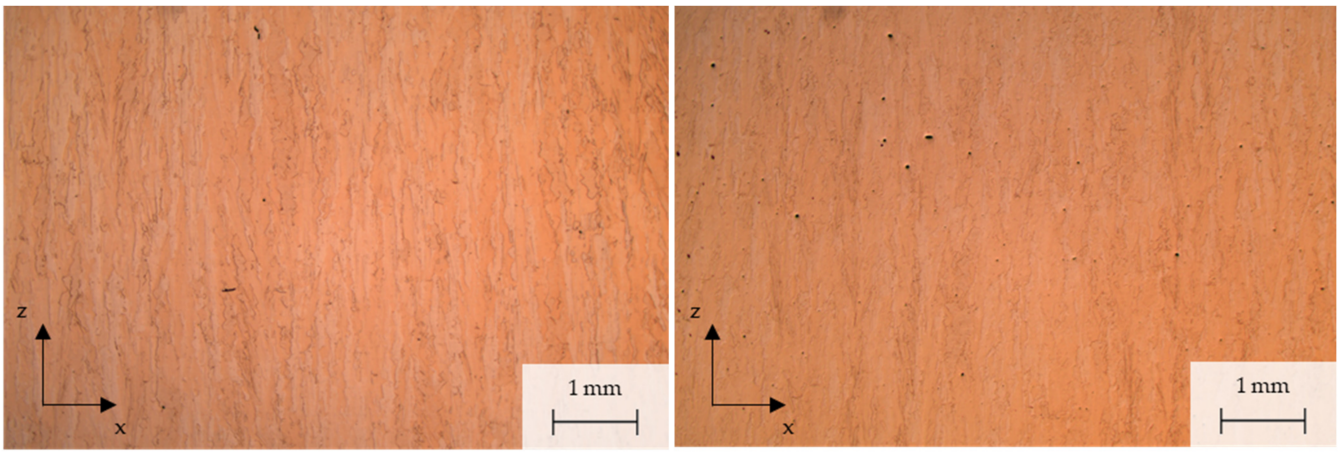

(**a**) (**b**)

Figure 7. *Cont.*

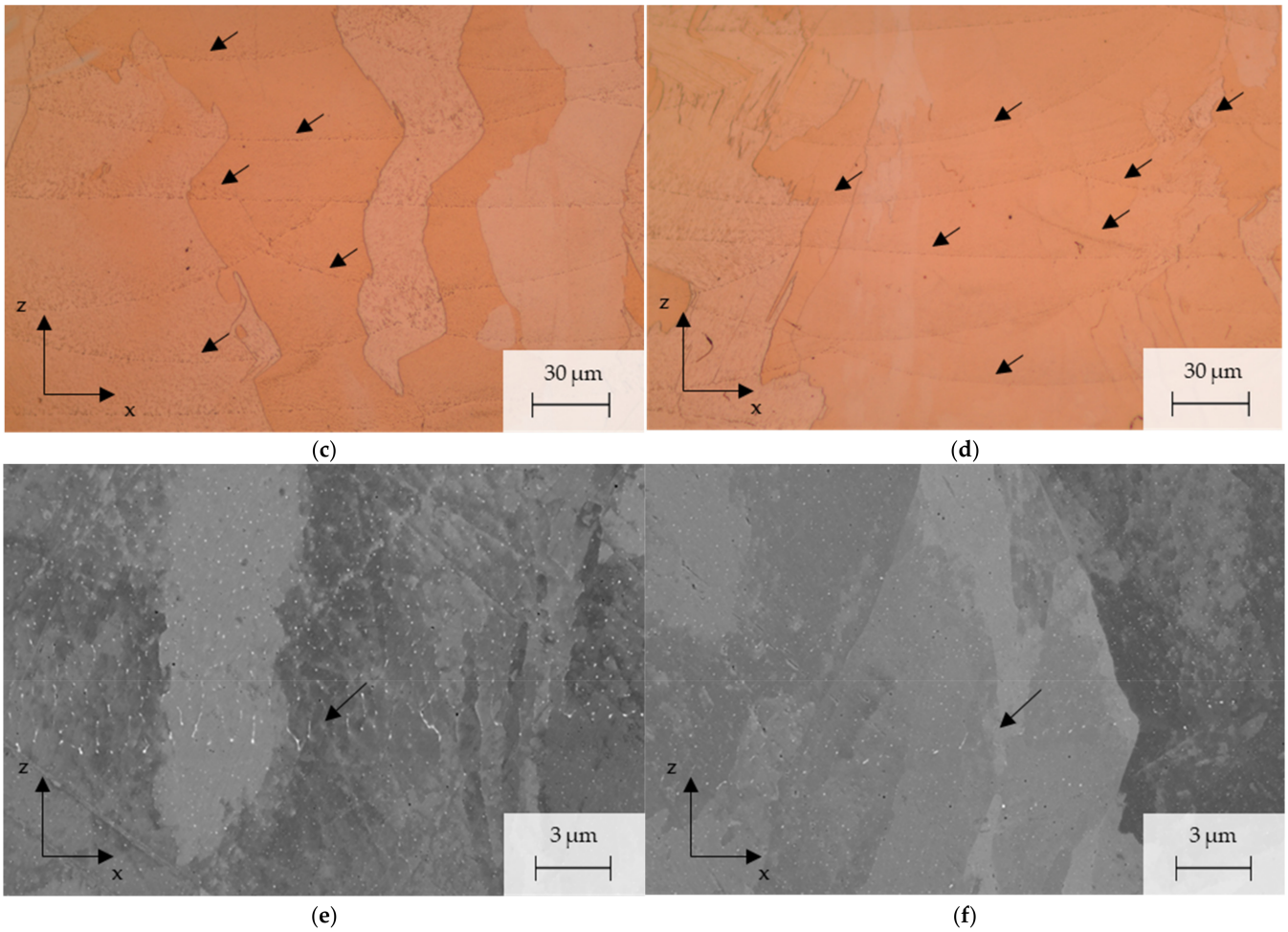

Figure 7. Microstructure in cross section of the x-z plane of additively manufactured CuHf0.7Cr0.35 with closed core pores during manufacturing (**a**,**b**). Resulting microstructure for manufacturing parameter sets A (**a**,**c**,**e**) and B (**b**,**d**,**f**) with visible traces of remelting by the AM laser marked with arrows (**c**–**f**).

During the manufacturing process and remelting of the powder material, Hf-containing phases visible in brighter contrast in Figure 7e,f sank downwards in the melt pool due to their higher density and gravitational forces. As a result, melting traces with a higher concentration of Hf-containing phases (see Appendix A Figure A2) at the lower region and a continuous transition in higher regions (arrows in Figure 7c–f) were visible. This phenomenon was more evident for parameter set A (Figure 7c,e in comparison to Figure 7d,f). Due to a lower scanning speed and consequently a higher energy density, the melt pool was larger and longer in the liquid state compared to parameter set B. As a result, phases with higher density had more time to sink and segregate.

After solution annealing, the microstructure was significantly changed with full recrystallization and a further dissolving of foreign phases. Figure 8 shows the microstructure for both AM parameter sets A and B. Grain boundaries formed during the annealing process, melting traces dissolved, and, as a result, further alloying element solubilized in the copper crystals. Some Cr-containing (Figure 8c,d (1)) or Hf-containing (Figure 8d (2)) phases formed at grain boundaries.

Regarding the measured electrical conductivity, a systematic influence was recognizable with a slightly lower conductivity after solution annealing in Figure 9. Within the annealing process, alloying elements dissolved in the copper crystal, which were initially present in individual phases within the powder and the as-built condition. By dissolving foreign atoms, the movement of conduction electrons is significantly hindered and the

conductivity decreases. Overall, the conductivity decreased from about 0.5 MS/m (parameter set B) to 1.1 MS/m (parameter set A), indicating an already quite good solution of alloying elements in the as-built condition. Nevertheless, the solution annealing process had a statistically significant influence regarding the electrical conductivity and highly correlated with the conducted metallographic investigations.

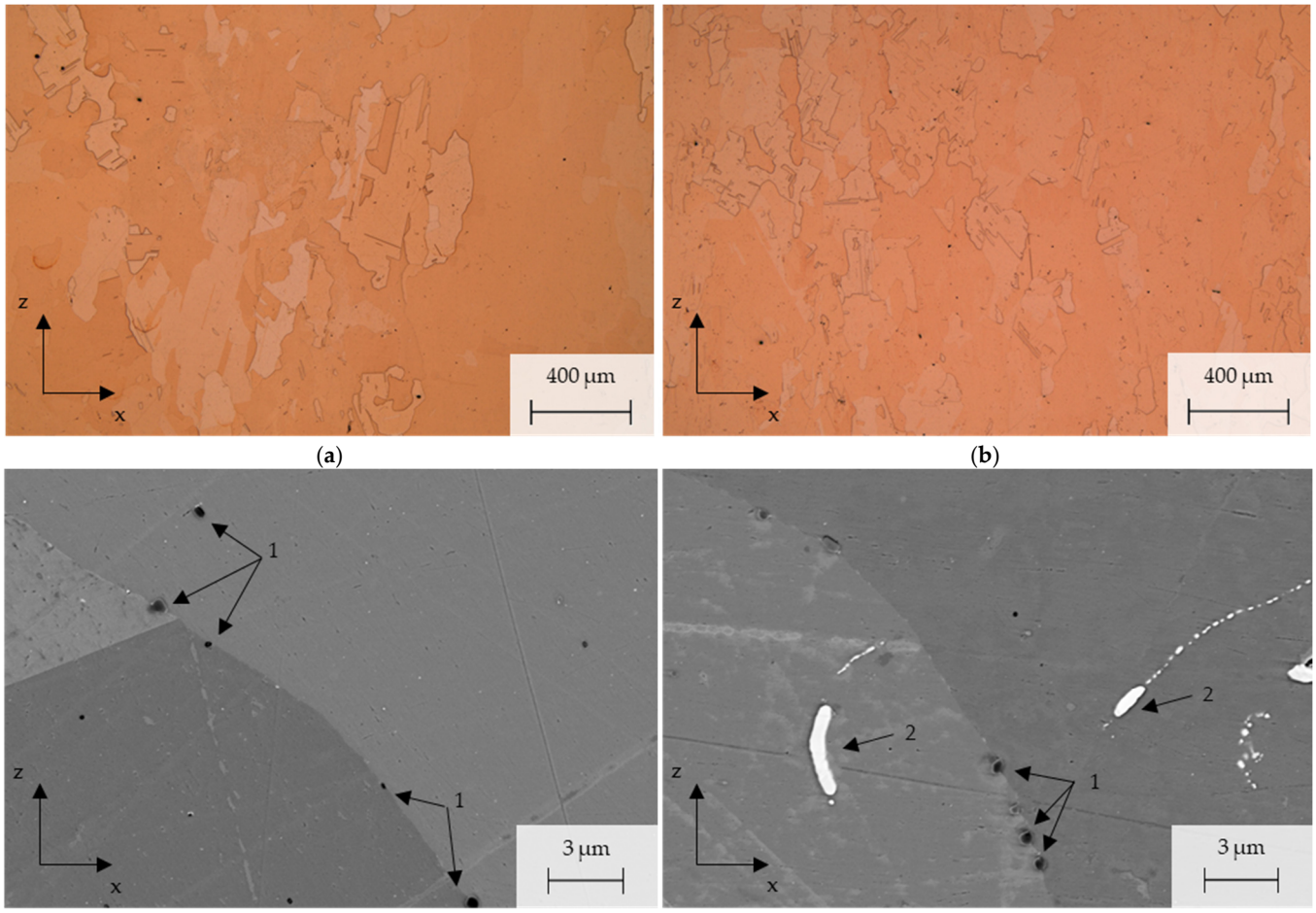

Figure 8. Microstructure in cross section of the x-z plane of additively manufactured CuHf0.7Cr0.35 after 70 min solution annealing at 970 °C. Full recrystallization (**a**,**b**) during the solution and homogenization process (**c**,**d**). Some Cr-containing phases (1) and Hf-containing (2) phases which were not solute during the annealing process.

In the as-built condition, CuCr1Zr provides electrical conductivities of about 12–14 MS/m [55,62] which is lower but at a comparable magnitude with the measured data of CuHfCr in this study.

In direct comparison, the as-built condition of specimens manufactured with parameter set B had higher hardness values. This correlated with the investigated microstructure and electrical conductivity, as these specimens appeared to have more alloying elements in solid solution. During the additive manufacturing process with higher scanning speed and a resulting lower energy density, fewer Hf-rich phases were built and, therefore, the segregations along the melting tracks were of lower intention. Furthermore, the electrical conductivity of these specimens was slightly lower, indicating a higher concentration of solute alloying elements. The solute alloying atoms in the copper matrix and their influence within the interaction of hardening mechanisms resulted in measurable differences in the as-built condition hardness levels.

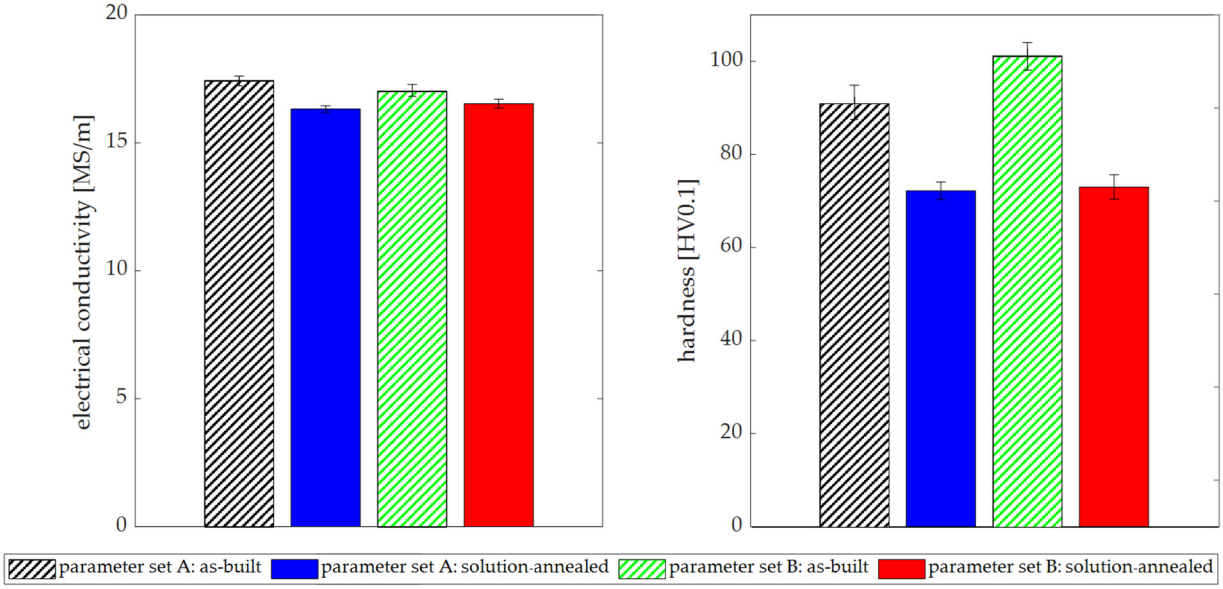

Figure 9. Influence of solution annealing on hardness and conductivity of additively manufactured CuHf0.7Cr0.35.

After solution annealing, both parameter sets resulted with a comparable hardness level of about 72 HV0.1. As visualized in Figure 9, the hardness of both parameter sets decreased by about 18 HV0.1 to 28 HV0.1 during the heat treatment with an entirely newly built microstructure (see Figure 8). During the annealing process, several hardening mechanisms interacted and contributed to the overall measured value in dynamically changing amounts. As shown with the electrical conductivity and metallographic investigations, the contribution of solid solution hardening increased with conducting the annealing process. Nevertheless, the overall hardness value was significantly reduced in comparison with the as-built condition which indicates a high contribution of further mechanisms. In the initial as-built condition, the contribution of small and distributed hard intermetallic phases (visible in the melting traces of Figure 7) needs to be considered as well.

Compared to die-cast bars with 75 HV0.1 hardness and 15 MS/m conductivity after solution annealing, the as-built specimens had a significantly higher hardness and slightly higher conductivity. After solution annealing the hardness and conductivity levels were nearly equal, referring to a comparable supersaturated solid solution condition.

In the as-built condition, additively manufactured CuCr1Zr specimens provide hardness values of about 90 HV1 [46,55,62], which is lower but at a comparable magnitude with the measured data for CuHfCr in this study. After solution annealing, this benchmark alloy provides about 65 HV [46], which is lower than the referring as-built condition as well.

3.3. Investigation of the Aged Conditions

In general, the solution of alloying elements in the copper matrix and a reduced solubility at lower temperatures is a requirement for precipitation hardening. A sufficient supersaturated solid solution provides the potential for precipitation hardening in following aging treatments, as it was described in earlier publications for this alloy CuHf0.7Cr0.35 processed by casting [5,6].

Figure 10 visualizes the electrical conductivity in the as-built condition, after direct aging and after solution annealing as well as aging at 475 °C for different aging times. For all specimens, aging for 2 h resulted in a substantial increase in electrical conductivity due to precipitation reactions. Parameter sets A and B provided comparable values, with an average difference of about 0.36 MS/m without any systematic influences. Generally, directly aged specimens provided higher electrical conductivities compared to the prior solution-annealed versions. As already discussed, this effect can be related to a higher

absolute amount of solute alloying elements and more scattering of conduction electrons in the copper matrix due to the annealing process. With increasing aging time, the difference between resulting electrical conductivities after aging from the as-built and the solution-annealed conditions continuously became smaller. As precipitation reactions progressed, the electrical conductivity, which approximately followed a saturation in the aging curves, became less influenced by previous processing steps.

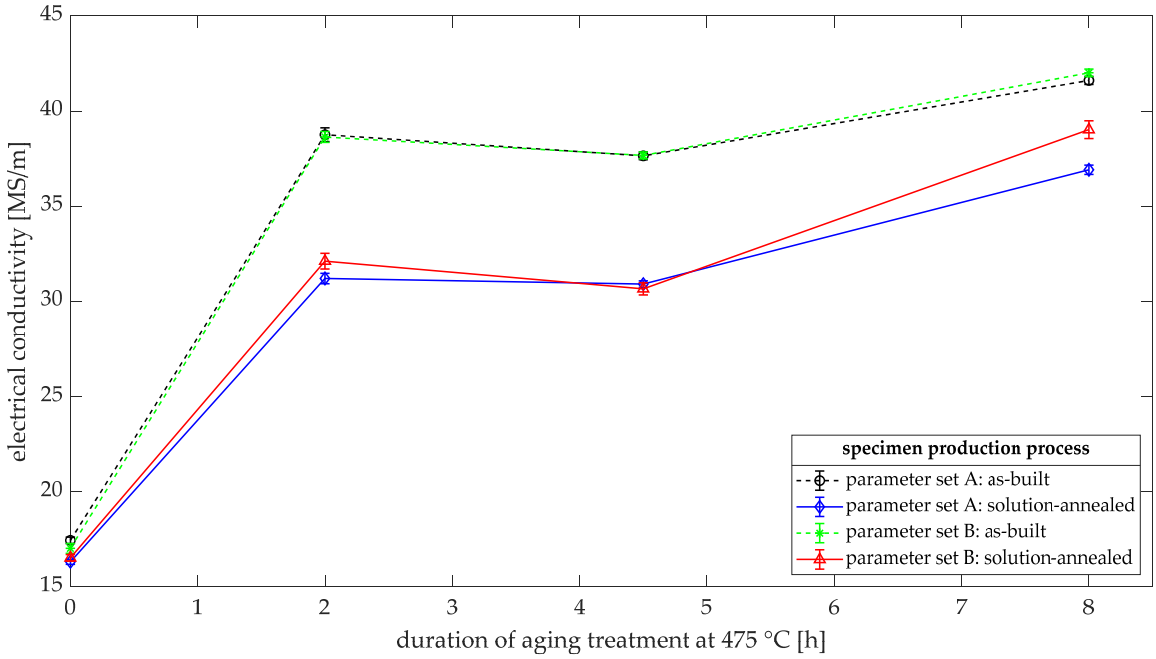

Figure 10. Influence of aging heat treatment on the electrical conductivities of CuHf0.7Cr0.35 in the as-built and solution-annealed (970 °C, 70 min) conditions.

Under comparable aging conditions, specimens of PBF-LB/M-processed CuCr1Zr alloys achieve conductivities of about 40–50 MS/m [46,55], which are in the lower range of the investigated alloy.

For CuHf0.7Cr0.35, further optimization of AM parameters and the heat treatment considering temperature and time could further optimize the properties of this alloy.

At a comparable aging temperature, this alloy in as-cast and solution-annealed conditions reached conductivities up to 40 MS/m after 8 h of aging time [5,6], which is comparable to the solution-annealed and additively aged manufactured specimens. With extended aging durations and further optimization of aging temperatures, an increase in the electrical conductivity can be realized up to 47 MS/m according to measurements of the comparable cast alloy [6].

Figure 11 visualizes the changes in hardness for directly aged as well as solution-annealed and aged conditions. As seen for the electrical conductivity, the hardness fits seamlessly into this development as well. Precipitation reactions started directly with the aging treatment and the hardness increased for all specimens. The solution-annealed specimens of both parameter sets A and B started with the same initial hardness level and developed with highly comparable properties during aging. Including the standard deviation, no statistically significant difference (according to Student's *t*-test) was recognizable. For the directly aged specimens, comparable hardness levels were measured after 2 h of aging. Parameter set B provided slightly higher hardness values in the case of the directly aged specimens. With regard to the metallographic and electrical conductivity investigations, this development perfectly supports the hypothesis of a slightly higher amount of solute alloying elements and higher supersaturation in the as-built condition for specimens with parameter set B compared to parameter set A. Due to the higher concentra-

tions of Cr and Hf atoms in the copper matrix of the as-built condition of parameter set B, there is consequently a higher potential for precipitation hardening throughout the whole following aging curve.

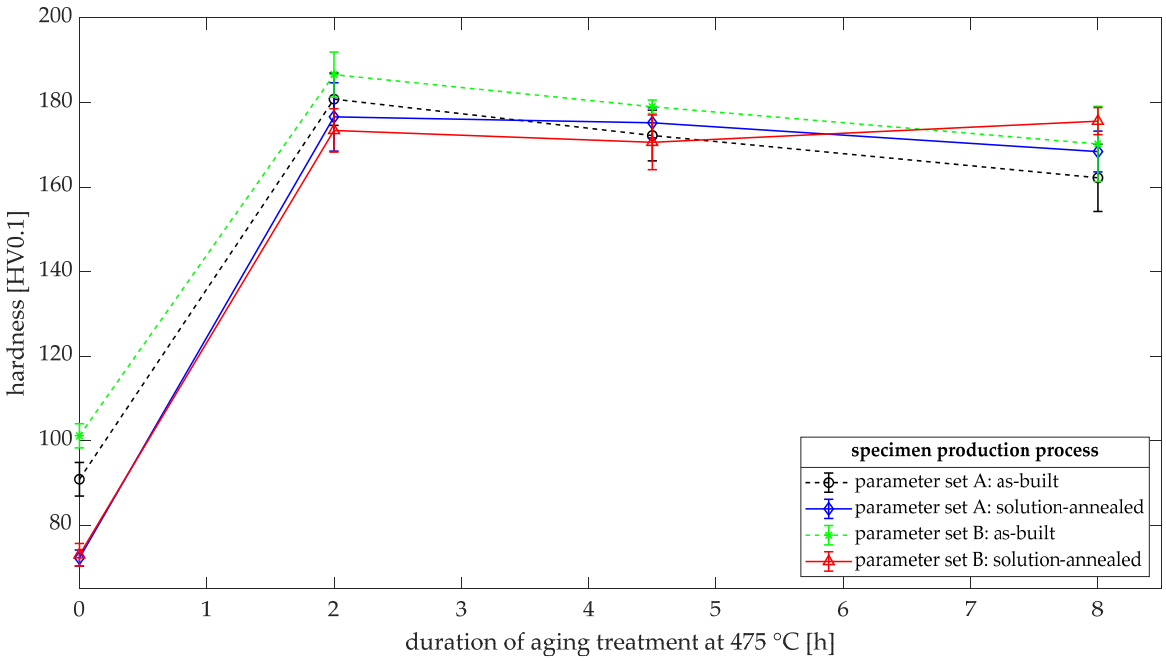

Figure 11. Influence of aging heat treatment on the hardness (HV0.1) of CuHf0.7Cr0.35 in the as-built and solution-annealed (970 °C, 70 min) conditions.

The initial hardness advantages of the as-built conditions compared to the solution-annealed conditions were reduced and the solution-annealed specimens reached comparable peak values after 2 h of aging. Overall, the specimens reached maximum hardness values of 173 HV0.1 to 187 HV0.1. After longer aging times, the hardness of directly aged specimens decreased. Solution annealed and aged specimens after 8 h of aging still reached about 170 HV0.1 to 175 HV0.1 in hardness compared to directly aged samples with only about 160 HV0.1 to 170 HV0.1. In order to utilize precipitation hardening, supersaturated solid solution is required, which was less prominent in the case of the directly aged specimens. As the precipitation reactions progressed and early-grown precipitates coarsened, the hardness level decreased. Regarding the mechanical properties, an initial solution annealing with the given AM process settings can be recommended in order to fully utilize the potent potential for precipitation hardening for this alloy.

Metallographic analysis of the aged specimens did not reveal further information about microstructural changes during the aging process. Figure 12 documents the aged conditions utilizing the parameter set A. In Figure 12a,c, no recrystallization effects in direct correlation with the as-built condition of Figure 7 are visible. Consequently, the melting tracks remained visible (arrows in Figure 12a) and these alloying elements could not contribute to precipitation reactions. During the powder remelting Hf-containing phases sank downwards in the melt pool due to their higher density (arrows in Figure 12c), resulting in these melting tracks. Arrows in Figure 12b visualize how prior solution annealing resulted in fully recrystallized grains but still some mainly Cr-rich phases could not be dissolved and did not contribute during the precipitation reaction as well (arrows in Figure 12d).

Regarding the visualization of precipitates in these aged conditions, SEM resolution is not sufficient as the precipitates were of small size ranges. High-resolution methods are necessary to understand the precipitation effects, which are mainly responsible for these changes in properties. Earlier precipitating mainly Cr-containing structures, transferred

from cast, solution annealed, and aged specimens, were presumably in the lower nanometer scale as well as the slightly larger growing contiguous intermetallic CuHf precipitates [5].

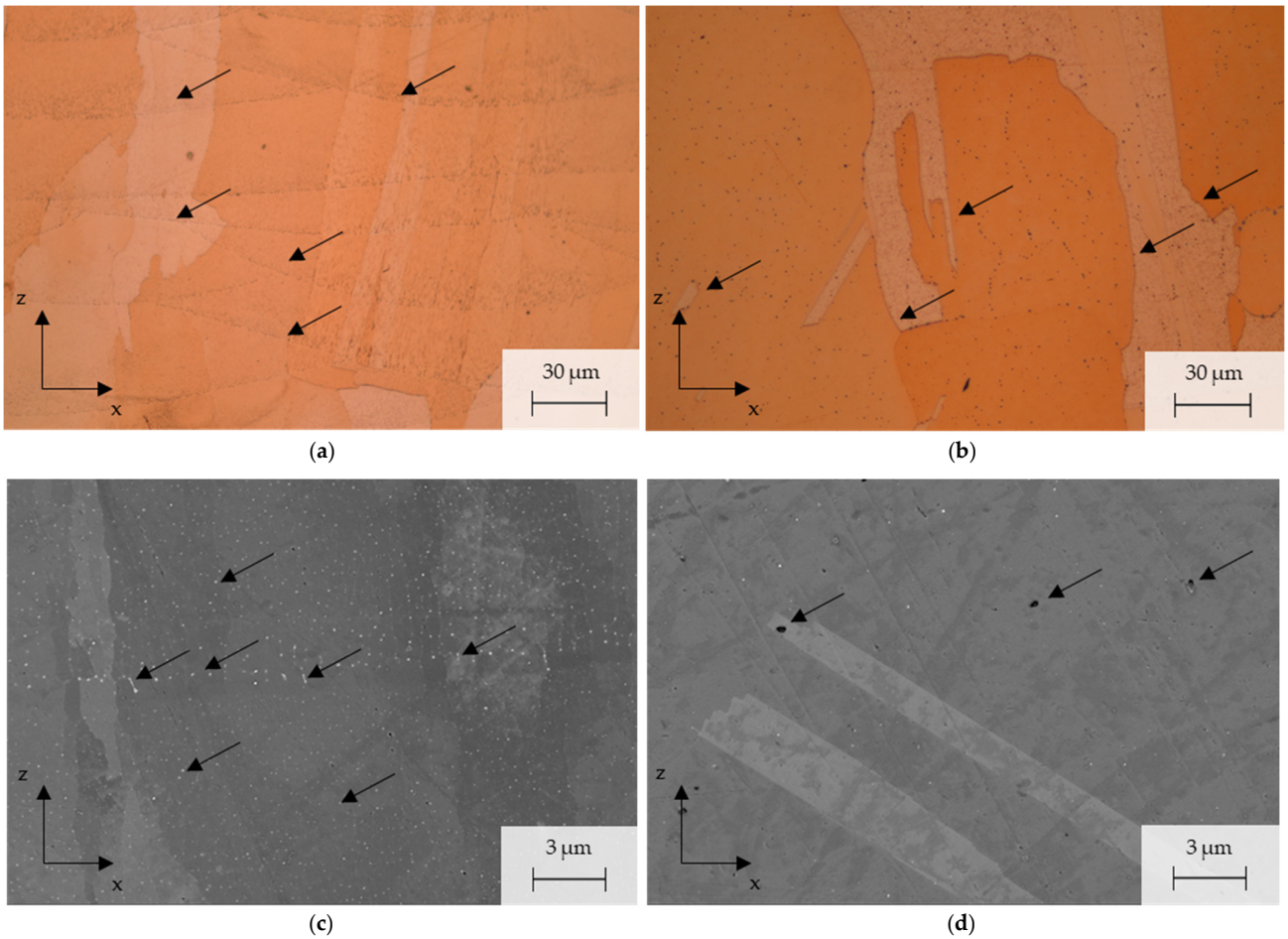

Figure 12. Microstructure in cross section of the x-z plane of additively manufactured CuHf0.7Cr0.35 (parameter set A) in aged conditions of 4.5 h at 475 °C. Directly aged as-built conditions (**a**,**c**) with melting tracks (arrows in (**a**)) and Hf-rich phases (arrows in (**c**)) in direct comparison to prior solution-annealed and quenched conditions (**b**,**d**) with fully recrystallized grains (arrows in (**b**)) and undissolved mainly Cr-rich phases (arrows in (**d**)).

Directly aged additively manufactured CuCr1Zr specimens provided hardness values of about 180–200 HV1 [55,62]. Overall, the additively manufactured specimens provided mechanical properties that were higher than the corresponding cast versions [62]. Parameter set B with faster scanning velocity is promising for further investigation and production. Generally, the introduction of higher energy densities (as was the case for parameter set A) carries a risk of higher melt temperatures and overheating, resulting in process instability and microstructural defects.

At a comparable aging temperature, the peak hardness for this alloy in a cast and solution-annealed condition was 190 HV0.1 [6], which is only 5 HV0.1 higher compared to the AM specimens and not statistically relevant. With further optimization of aging temperature and time, peak hardness values of up to 205 HV0.1 (aging at 400 °C for 2 h) have been reported for this cast alloy [5,6].

In direct comparison with other additively manufactured benchmark alloys, Figure 13 visualizes the analyzed properties of CuHf0.7Cr0.35. Regarding the conflicting objectives of high mechanical properties and high electrical conductivity, CuHf0.7Cr0.35 offers high potential. The alloy already impressed with good performance at elevated temperatures, especially in comparison to CuCr1Zr [6].

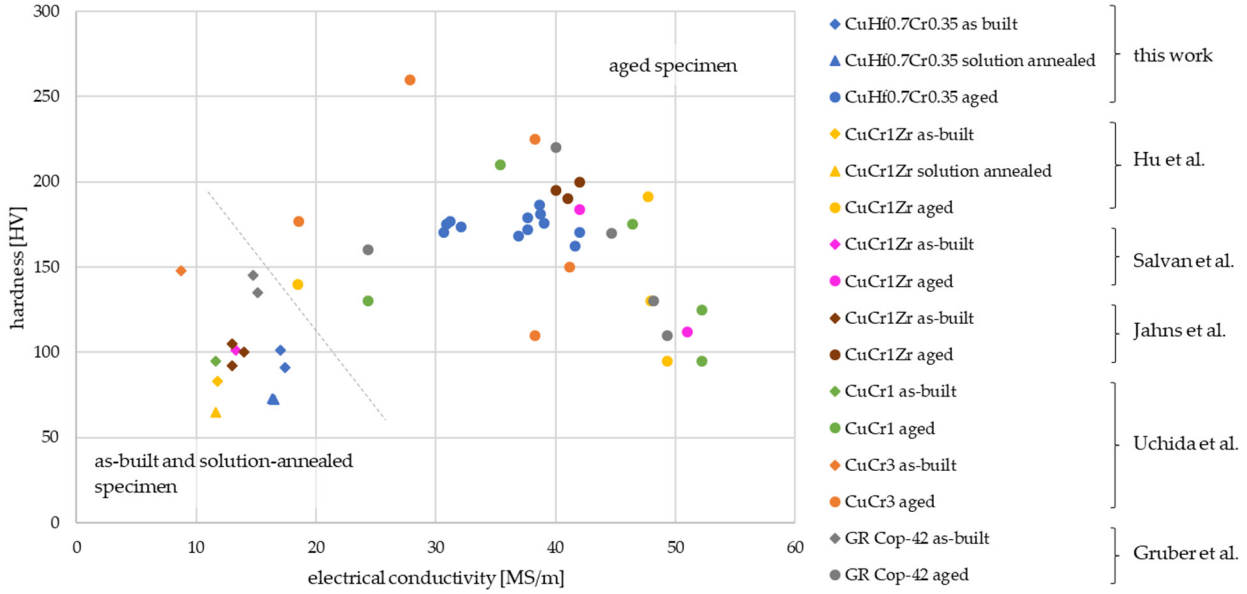

Figure 13. Overview of material property combinations regarding hardness and electrical conductivity for low-alloyed copper alloys (benchmark alloys: CuCr alloys, CuCr1Zr, GR Cop versions of [46,49,55,58,62]) in powder form manufactured via generative PBF-LB/M processes.

4. Conclusions

A low-alloyed copper alloy containing hafnium and chromium (CuHf0.7Cr0.35) was atomized and powder processed by PBF-LB/M for the first time in this study. Powder atomization, additive manufacturing, and subsequent aging treatments were successfully utilized to modify the properties of resulting material specimens:

1. Utilizing gas atomization, it was possible to produce spherical particles of CuHf0.7Cr0.35 with a D50 of approximately 33 µm after sieving and wind sifting. Some particles were attached with small satellites but were well suited for further additive manufacturing using PBF-LB/M.
2. Two different parameter sets for the generative manufacturing process were investigated, resulting in slight differences. Comparable density was reached with hardness values of about 100 HV0.1 and an electrical conductivity of 17 MS/m. In direct comparison of the parameter sets A and B, the chosen faster scanning velocity of parameter set B (laser power 500 W, laser scanning velocity 1100 mm/s, hatch distance 150 µm, and a layer thickness of 30 µm) is promising for industrial production. The lower energy density carries a reduced risk of high melt temperatures and overheating. Regarding an effective production method and reduced risk for microstructural defects, this parameter set B will be the starting point for further investigations.
3. Melting traces with phases of higher Hf content were visible in the microstructure but later dissolved during solution annealing at 970 °C for 70 min, including recrystallization. The resulting hardness values of 73 HV0.1 and 16 MS/m were comparable to cast and annealed versions of the investigated CuHf0.7Cr0.35 alloy.
4. Aging had a significant effect on the electrical conductivity and hardness of additively manufactured CuHf0.7Cr0.35. The directly aged specimens had lower alloying elements in their as-built condition. Due to a lower supersaturated solid solution, higher electrical conductivities of up to 42 MS/m were possible, whereas the solution-annealed versions reached about 38 MS/m after 8 h of aging. Nevertheless, during the aging treatment, several hardening mechanisms interacted simultaneously and the advantageous as-built condition was further exploited to peak hardness values of 187 HV0.1, whereas the solution-annealed starting condition achieved about 14 HV0.1 less.

5. The comparison with cast specimens with identical raw materials regarding electrical conductivity suggests further analysis of different aging temperatures and times to further explore the potential use of this PBF-LB/M-produced alloy.

Optimization of AM manufacturing parameters, optional annealing, aging temperature, and aging time could further enhance the potential of CuHf0.7Cr0.35. Future studies will concentrate on the AM production process itself, reuse of powder material, and reproducibility. Furthermore, target-oriented aging treatments to maximize the precipitating volume fraction and investigations regarding the high temperature behavior will be of importance.

Author Contributions: Conceptualization, J.D., S.G., E.B., E.L. and A.Z.; methodology, J.D., S.G. and F.K.; validation, J.D., S.G. and F.K.; formal analysis, J.D. and S.G.; investigation, J.D., S.G. and F.K.; resources, E.B., A.Z., L.S., E.L. and H.-G.W.; writing—original draft preparation, J.D. and S.G.; writing—review and editing, E.B., L.S., C.L., E.L., H.-G.W. and A.Z.; visualization, J.D. and S.G.; supervision, E.B., L.S., E.L., C.L. and A.Z. All authors have read and agreed to the published version of the manuscript.

Funding: This research received no external funding.

Data Availability Statement: The original contributions presented in the study are included in the article, further inquiries can be directed to the corresponding author.

Conflicts of Interest: The authors Felix Kovermann and Hans-Günther Wobker were employed by the company "cunova GmbH". The remaining authors declare that the research was conducted in the absence of any commercial or financial relationships that could be construed as potential conflicts of interest.

Appendix A

To visualize the elementary distribution of copper, hafnium, and chromium within an exemplary microstructure of a powder particle, Figure A1 shows the results of EDS scanning in direct comparison to the backscatter detector image. Higher concentrations of Hf atoms in Hf-containing intermetallic phases became visible in brighter contrast in the BSD detector. The Cr content was homogenously distributed over the whole cross-section.

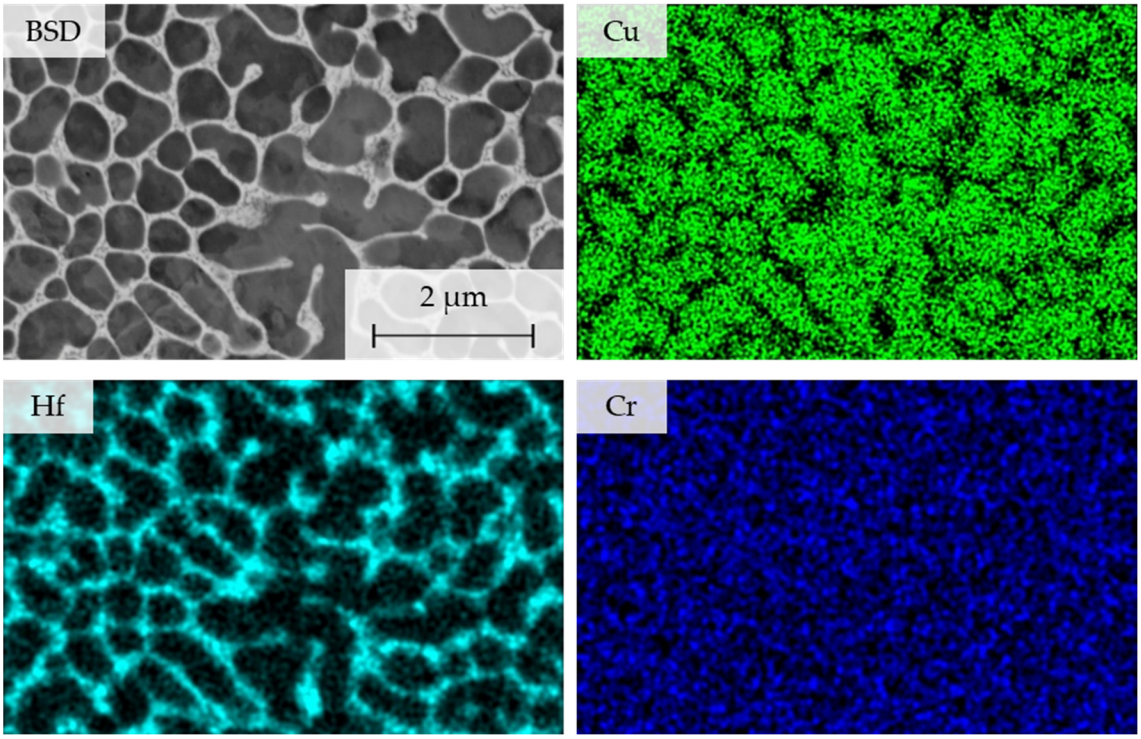

Figure A1. Cross-section of CuHf0.7Cr0.35 powder particle in SEM investigation: BSD image and results from EDS scanning (EDS signal amplified).

In the as-built condition of additively manufactured specimens of CuHf0.7Cr0.35, melting tracks were visible in the microstructure. Accumulations of phases containing a higher Hf content are visible in Figure A2, visualized with corresponding EDS scanning (arrows).

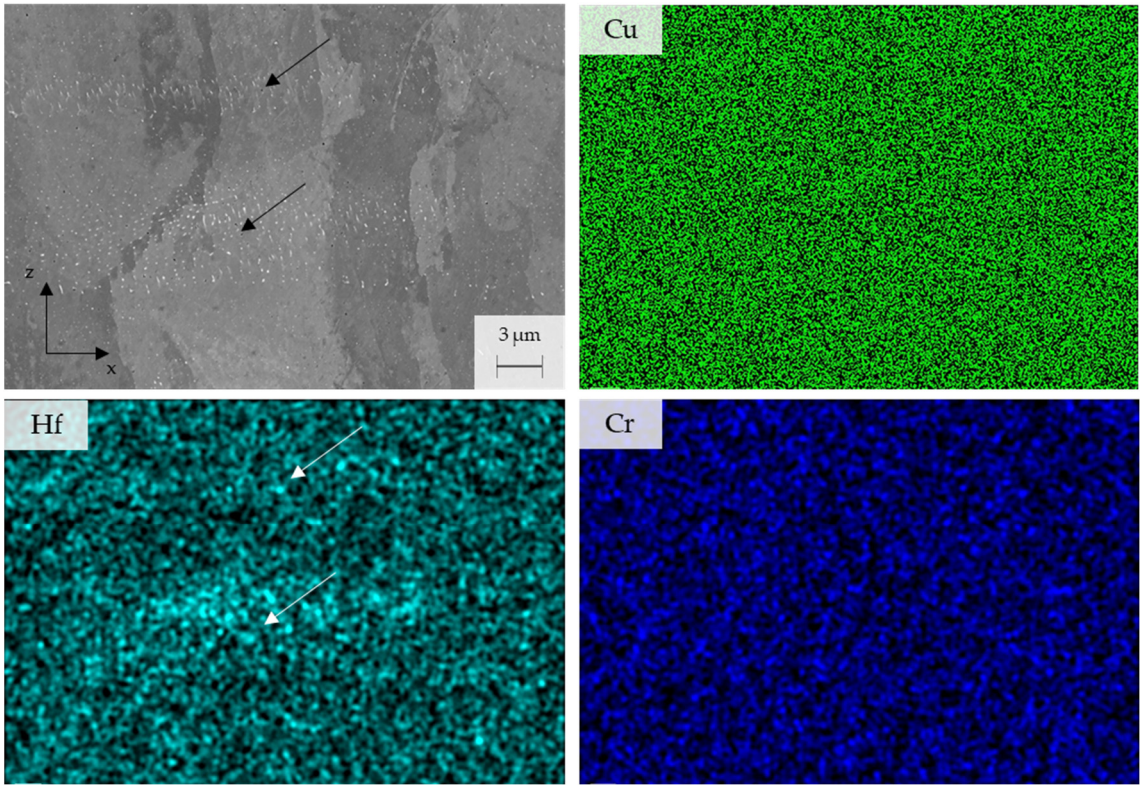

Figure A2. Cross-section of CuHf0.7Cr0.35 in an additively manufactured as-built condition (parameter set A) in SEM investigation: BSD image and results from EDS scanning (EDS signal amplified) with melting tracks, resulting in segregation of Hf-rich phases (arrows).

References

1. Porter, D.A.; Easterling, K.E.; Sherif, M.Y. (Eds.) *Phase Transformations in Metals and Alloys*, 4th ed.; CRC Press: Boca Raton, FL, USA, 2021; ISBN 978-1-00301-180-4.
2. Dies, K. *Kupfer und Kupferlegierungen in der Technik*; Springer: Berlin/Heidelberg, Germany, 2014; ISBN 978-3-642-48932-7.
3. Davis, J.R. *Metals Handbook: Non-Ferrous Alloys and Special-Purpose Materials*, 10th ed.; ASM International: Ohio, OH, USA, 1990; ISBN 0-871-70378-5.
4. Gottstein, G. *Materialwissenschaft und Werkstofftechnik: Physikalische Grundlagen*, 4th ed.; Springer: Berlin/Heidelberg, Germany, 2014; ISBN 978-3-642-36602-4.
5. Dölling, J.; Kuglstatter, M.; Prahl, U.; Höppel, H.W.; Ortner, P.; Ott, B.; Kracun, S.F.; Fehlbier, M.; Zilly, A. Analyzing the Precipitation Effects in Low-Alloyed Copper Alloys Containing Hafnium and Chromium. *Metals* **2024**, *14*, 258. [CrossRef]
6. Dölling, J. *Niedriglegierte Kupferlegierungen mit Hafnium und Scandium für Erhöhte Mechanische Anforderungen*, 1st ed.; Technische Universität Bergakademie Freiberg: Freiberg, Germany, 2024; ISBN 3-86012-714-4.
7. Martynenko, N.; Rybalchenko, O.; Straumal, P.; Tabachkova, N.; Lukyanova, E.; Rybalchenko, G.; Prosvirnin, D.; Beletsky, E.; Prokofiev, P.; Yusupov, V.; et al. Increasing strength and electrical conductivity of Cu-0.77%Cr-0.86%Hf alloy by rotary swaging and subsequent aging. *J. Mater. Sci.* **2024**, *59*, 5944–5955. [CrossRef]
8. Chakrabarti, D.J.; Laughlin, D.E. The Cr-Cu (Chromium-Copper) system. *Bull. Alloy Phase Diagr.* **1984**, *5*, 59–68. [CrossRef]
9. Li, M.; Zhang, L.; Zhu, M.; Wang, H.; Wei, H. Physical Properties and Precipitate Microstructures of Cu-Hf Alloys at Different Processing Stages. *Scanning* **2018**, *2018*, 3653987. [CrossRef] [PubMed]
10. Li, H.; XIE, S.; WU, P.; Mi, X. Study on improvement of conductivity of Cu-Cr-Zr alloys. *Rare Met.* **2007**, *26*, 124–130. [CrossRef]
11. Peng, L.; Xie, H.; Huang, G.; Xu, G.; Yin, X.; Feng, X.; Mi, X.; Yang, Z. The phase transformation and strengthening of a Cu-0.71 wt% Cr alloy. *J. Alloys Compd.* **2017**, *708*, 1096–1102. [CrossRef]
12. Freudenberger, J.; Heilmaier, M. *Materialkunde der Nichteisenmetalle und -Legierungen*, 1st ed.; Wiley-VCH Verlag GmbH & Co. KGaA: Weinheim, Germany, 2020; ISBN 978-3-52782-254-6.

13. Liu, J.; Hou, M.; Yang, H.; Xie, H.; Yang, C.; Zhang, J.; Feng, Q.; Wang, L.; Meng, L.; Wang, H. In-situ TEM study of the dynamic interactions between dislocations and precipitates in a Cu-Cr-Zr alloy. *J. Alloys Compd.* **2018**, *765*, 560–568. [CrossRef]
14. Wan, X.; Xie, W.; Chen, H.; Tian, F.; Wang, H.; Yang, B. First-principles study of phase transformations in Cu–Cr alloys. *J. Alloys Compd.* **2021**, *862*, 158531. [CrossRef]
15. Bodyakova, A.; Mishnev, R.; Belyakov, A.; Kaibyshev, R. Effect of chromium content on precipitation in Cu–Cr–Zr alloys. *J. Mater. Sci.* **2022**, *57*, 13043–13059. [CrossRef]
16. Chbihi, A.; Sauvage, X.; Blavette, D. Atomic scale investigation of Cr precipitation in copper. *Acta Mater.* **2012**, *60*, 4575–4585. [CrossRef]
17. Holzwarth, U.; Stamm, H. The precipitation behaviour of ITER-grade Cu–Cr–Zr alloy after simulating the thermal cycle of hot isostatic pressing. *J. Nucl. Mater.* **2000**, *279*, 31–45. [CrossRef]
18. Hatakeyama, M.; Toyama, T.; Yang, J.; Nagai, Y.; Hasegawa, M.; Ohkubo, T.; Eldrup, M.; Singh, B.N. 3D-AP and positron annihilation study of precipitation behavior in Cu–Cr–Zr alloy. *J. Nucl. Mater.* **2009**, *386–388*, 852–855. [CrossRef]
19. Chenna Krishna, S.; Radhika, K.V.; Tharian, K.T.; Swathi Kiranmayee, M.; Sudarshan Rao, G.; Jha, A.K.; Pant, B. Dynamic Embrittlement in Cu-Cr-Zr-Ti Alloy: Evidence of Intergranular Segregation of Sulphur. *J. Mater. Eng. Perform.* **2013**, *22*, 2331–2336. [CrossRef]
20. Zhang, S.; Li, R.; Kang, H.; Chen, Z.; Wang, W.; Zou, C.; Li, T.; Wang, T. A high strength and high electrical conductivity Cu-Cr-Zr alloy fabricated by cryorolling and intermediate aging treatment. *Mater. Sci. Eng. A* **2017**, *680*, 108–114. [CrossRef]
21. Fuxiang, H.; Jusheng, M.; Honglong, N.; Zhiting, G.; Chao, L.; Shumei, G.; Xuetao, Y.; Tao, W.; Hong, L.; Huafen, L. Analysis of phases in a Cu–Cr–Zr alloy. *Scr. Mater.* **2003**, *48*, 97–102. [CrossRef]
22. Tang, N.Y.; Taplin, D.M.R.; Dunlop, G.L. Precipitation and aging in high-conductivity Cu–Cr alloys with additions of zirconium and magnesium. *Mater. Sci. Technol.* **1985**, *1*, 270–275. [CrossRef]
23. Langner, R.; Rust, K. Herstellung und Eigenschaften von CuCr und CuCrZr. Mitteilung aus dem VEB Vereinigte NE-Metall-Halbzeugwerke Hettstedt. *Neue Hütte Metall.-Met. Fachz. Für Forsch. Prax.* **1967**, *12*, 550–555.
24. Batra, I.S.; Dey, G.K.; Kulkarni, U.D.; Banerjee, S. Precipitation in a Cu–Cr–Zr alloy. *Mater. Sci. Eng. A* **2003**, *356*, 32–36. [CrossRef]
25. Saarivirta, M.J. High conductivity copper alloys—Part 1. *Met. Ind.* **1963**, *103*, 685–688.
26. Yang, Y.; Kuang, G.; Li, R. Optimizing the Electrical and Mechanical Properties of Cu-Cr Alloys by Hf Microalloying. *Metals* **2022**, *12*, 485. [CrossRef]
27. Shangina, D.V.; Bochvar, N.R.; Dobatkin, S.V. The effect of alloying with hafnium on the thermal stability of chromium bronze after severe plastic deformation. *J. Mater. Sci.* **2012**, *47*, 7764–7769. [CrossRef]
28. Dobatkin, S.V.; Shangina, D.V.; Bochvar, N.R.; Terent'ev, V.F.; Prosvirnin, D.V.; Putinceva, M.N.; Purcek, G.; Yanar, H.; Alsaran, A.; Raab, G.I. Enhanced mechanical and service properties of ultrafinegrained copper-based alloys with Cu, Zr and Hf additives. *Mater. Sci. Non-Equilib. Phase Transform.* **2017**, *3*, 3–5.
29. Jiang, Y.; Zhang, X.; Cai, P.; Li, P.; Cao, F.; Gao, F.; Liang, S. Precipitation behavior and microstructural evolution during thermo-mechanical processing of precipitation hardened Cu-Hf based alloys. *Acta Mater.* **2023**, *245*, 118659. [CrossRef]
30. Yi, G.; Zhang, X.; Qin, J.; Ning, J.; Zhang, S.; Ma, M.; Liu, R. Mechanical, electronic and thermal properties of Cu5Zr and Cu5Hf by first-principles calculations. *J. Alloys Compd.* **2015**, *640*, 455–461. [CrossRef]
31. Saarivirta, M.J. High conductivity copper alloys—Part 2. *Met. Ind.* **1963**, *103*, 716–718.
32. Saarivirta, M.J. High conductivity copper alloys—Part 3. *Met. Ind.* **1963**, *103*, 758–760.
33. Ghosh, G. First-principles calculations of structural energetics of Cu–TM (TM = Ti, Zr, Hf) intermetallics. *Acta Mater.* **2007**, *55*, 3347–3374. [CrossRef]
34. Bochvar, N.R.; Rybalchenko, O.V.; Shangina, D.V.; Dobatkin, S.V. Effect of equal-channel angular pressing on the precipitation kinetics in Cu-Cr-Hf alloys. *Mater. Sci. Eng. A* **2019**, *757*, 84–87. [CrossRef]
35. Li, R.; Zhang, S.; Zou, C.; Kang, H.; Wang, T. The roles of Hf element in optimizing strength, ductility and electrical conductivity of copper alloys. *Mater. Sci. Eng. A* **2019**, *758*, 130–138. [CrossRef]
36. Rybalchenko, O.V.; Bochvar, N.R.; Rybalchenko, G.V.; Martynenko, N.S.; Tabachkova, N.Y.; Dobatkin, S.V. Comparative analysis of the aging kinetics in low-alloyed Cu–Cr–Hf and Cu–Cr–Zr alloys after high pressure torsion. *J. Alloys Compd.* **2023**, *955*, 170246. [CrossRef]
37. Shangina, D.V.; Ivanov, N.I.; Bochvar, N.R.; Dobatkin, S.V. Resistance of the Contact Welding Electrodes Made of a Cu–0.7% Cr–0.9% Hf Alloy with an Ultrafine-Grained Structure. *Russ. Metal.* **2018**, *2018*, 815–819. [CrossRef]
38. Shangina, D.; Maksimenkova, Y.; Bochvar, N.; Serebryany, V.; Raab, G.; Vinogradov, A.; Skrotzki, W.; Dobatkin, S. Influence of alloying with hafnium on the microstructure, texture, and properties of Cu–Cr alloy after equal channel angular pressing. *J. Mater. Sci.* **2016**, *51*, 5493–5501. [CrossRef]
39. Shangina, D.; Maksimenkova, Y.; Bochvar, N.; Serebryany, V.; Raab, G.; Vinogradov, A.; Skrotzki, W.; Dobatkin, S. Structure and Properties of Cu Alloys Alloying with Cr and Hf after Equal Channel Angular Pressing. *AMR* **2014**, *922*, 651–656. [CrossRef]
40. Shangina, D.V.; Terent'ev, V.F.; Prosvirnin, D.V.; Antonova, O.V.; Bochvar, N.R.; Gorshenkov, M.V.; Raab, G.I.; Dobatkin, S.V. Mechanical Properties, Fatigue Life, and Electrical Conductivity of Cu-Cr-Hf Alloy after Equal Channel Angular Pressing. *Adv. Eng. Mater.* **2018**, *20*, 1700536. [CrossRef]
41. Tang, X.; Chen, X.; Sun, F.; Liu, P.; Zhou, H.; Fu, S. The current state of CuCrZr and CuCrNb alloys manufactured by additive manufacturing: A review. *Mater. Des.* **2022**, *224*, 111419. [CrossRef]

42. Gruber, S.; Stepien, L.; López, E.; Brueckner, F.; Leyens, C. Physical and Geometrical Properties of Additively Manufactured Pure Copper Samples Using a Green Laser Source. *Materials* **2021**, *14*, 3642. [CrossRef] [PubMed]
43. Tiberto, D.; Klotz, U.E.; Held, F.; Wolf, G. Additive manufacturing of copper alloys: Influence of process parameters and alloying elements. *Mater. Sci. Technol.* **2019**, *35*, 969–977. [CrossRef]
44. Schmidt, M.; Merklein, M.; Bourell, D.; Dimitrov, D.; Hausotte, T.; Wegener, K.; Overmeyer, L.; Vollertsen, F.; Levy, G.N. Laser based additive manufacturing in industry and academia. *CIRP Ann.* **2017**, *66*, 561–583. [CrossRef]
45. Popovich, A.; Sufiiarov, V.; Polozov, I.; Borisov, E.; Masaylo, D.; Orlov, A. Microstructure and mechanical properties of additive manufactured copper alloy. *Mater. Lett.* **2016**, *179*, 38–41. [CrossRef]
46. Hu, Z.; Liu, Z.; Ma, T.; Gao, Z.; Gan, B.; Ma, Z.; Liu, Y. Achieving High Strength and High Electrical Conductivity of Additive Manufactured CuCrZr Alloys: The Role of the Post-Heat Treatments on Microstructure and Properties. *Metall. Mat. Trans. A* **2023**, *54*, 4306–4314. [CrossRef]
47. Colopi, M.; Demir, A.G.; Caprio, L.; Previtali, B. Limits and solutions in processing pure Cu via selective laser melting using a high-power single-mode fiber laser. *Int. J. Adv. Manuf. Technol.* **2019**, *104*, 2473–2486. [CrossRef]
48. Wagenblast, P.; Myrell, A.; Thielmann, M.; Scherbaum, T.; Coupek, D. Additive manufacturing with green disk lasers. In *Laser 3D Manufacturing VII, Proceedings of the SPIE LASE, San Francisco, CA, USA, 1–6 February 2020*; Helvajian, H., Gu, B., Chen, H., Eds.; SPIE: Bellingham, WA, USA, 2020; p. 18. ISBN 978-1-51063-305-6.
49. Uchida, S.; Kimura, T.; Nakamoto, T.; Ozaki, T.; Miki, T.; Takemura, M.; Oka, Y.; Tsubota, R. Microstructures and electrical and mechanical properties of Cu-Cr alloys fabricated by selective laser melting. *Mater. Des.* **2019**, *175*, 107815. [CrossRef]
50. Fraunhofer Gesellschaft, e.V. *Fraunhofer-Institut für Lasertechnik ILT. Schlussbericht zu IGF-Vorhaben Nr. 19.549 N: Additive Fertigung von Bauteilen aus Rein-Kupfer mittels SLM und "grüner" Laserstrahlung*; Industrielle Gemeinschaftsforschung: Aachen, Germany, 2020.
51. Buchholz, M.; Gruber, S.; Selbmann, A.; Marquardt, A.; Meier, L.; Müller, M.; Seifert, L.; Leyens, C.; Tajmar, M.; Bach, C. Flow rate improvements in additively manufactured flow channels suitable for rocket engine application. *CEAS Space J.* **2023**, *15*, 715–728. [CrossRef]
52. Gradl, P.; Greene, S.; Protz, C.; Bullard, B.; Buzzell, J.; Garcia, C.; Wood, J.; Cooper, K.; Hulka, J.; Osborne, R. Additive Manufacturing of Liquid Rocket Engine Combustion Devices: A Summary of Process Developments and Hot-Fire Testing Results. In Proceedings of the 2018 Joint Propulsion Conference, Cincinnati, OH, USA, 9–11 July 2018.
53. Morshed-Behbahani, K.; Aliyu, A.; Bishop, D.P.; Nasiri, A. Additive manufacturing of copper-based alloys for high-temperature aerospace applications: A review. *Mater. Today Commun.* **2024**, *38*, 108395. [CrossRef]
54. Wallis, C.; Buchmayr, B. Effect of heat treatments on microstructure and properties of CuCrZr produced by laser-powder bed fusion. *Mater. Sci. Eng. A* **2019**, *744*, 215–223. [CrossRef]
55. Salvan, C.; Briottet, L.; Baffie, T.; Guetaz, L.; Flament, C. CuCrZr alloy produced by laser powder bed fusion: Microstructure, nanoscale strengthening mechanisms, electrical and mechanical properties. *Mater. Sci. Eng. A* **2021**, *826*, 141915. [CrossRef]
56. Ellis, D.L. *GRCop-84: A High-Temperature Copper Alloy for High-Heat-Flux Applications: 213566*; NASA Glenn Research Center: Cleveland, OH, USA, 2005.
57. de Groh, H.C.; Ellis, D.L.; Loewenthal, W.S. Comparison of GRCop-84 to Other Cu Alloys with High Thermal Conductivities. *J. Mater. Eng. Perform.* **2008**, *17*, 594–606. [CrossRef]
58. Gruber, S.; Stepien, L.; Gerdt, L.; Lopez, E.; Kieser, J.; Brueckner, F.; Leyens, C.; Bratt, C. Process development for laser powder bed fusion of GRCop-42 using a 515 nm laser source. *J. Laser Appl.* **2023**, *35*, 042078. [CrossRef]
59. deGroh, H., III; Ellis, D.; Loewenthal, W. *Comparison of GRCop-84 to Other High Thermal Conductive Cu Alloys*; NASA STI Program; NASA Glenn Research Center: Cleveland, OH, USA, 2007.
60. Gradl, P.R.; Protz, C.S.; Cooper, K.; Ellis, D.; Evans, L.J.; Garcia, C. GRCop-42 Development and Hot-fire Testing Using Additive Manufacturing Powder Bed Fusion for Channel-cooled Combustion Chambers. In Proceedings of the AIAA Propulsion and Energy 2019 Forum, Indianapolis, IN, USA, 19–22 August 2019; American Institute of Aeronautics and Astronautics: Reston, VA, USA, 2019.
61. Dölling, J.; Henle, R.; Prahl, U.; Zilly, A.; Nandi, G. Copper-Based Alloys with Optimized Hardness and High Conductivity: Research on Precipitation Hardening of Low-Alloyed Binary CuSc Alloys. *Metals* **2022**, *12*, 902. [CrossRef]
62. Jahns, K.; Bappert, R.; Böhlke, P.; Krupp, U. Additive manufacturing of CuCr1Zr by development of a gas atomization and laser powder bed fusion routine. *Int. J. Adv. Manuf. Technol.* **2020**, *107*, 2151–2161. [CrossRef]
63. *DIN ISO 6507-1:2018*; Metallic Materials—Vickers Hardness Test—Part 1: Test Method; German Version EN ISO 6507-1:2018. DIN Media GmbH: Berlin, Germany, 2018. [CrossRef]
64. Petzow, G. *Metallographisches, Keramographisches, Plastographisches Ätzen*, 7th ed.; Gebrüder Borntraeger: Stuttgart, Germany, 2015; ISBN 978-3-44323-019-7.
65. *ISO 13322-2*; Particle Size Analysis—Image Analysis Methods—Part 2: Dynamic Image Analysis Methods. DIN Media GmbH: Berlin, Germany, 2021.